Multidimensional Synergistic Nanoarchitecture Exhibiting Highly Stable and Ultrafast Sodium-Ion Storage

Shuangshuang Tan, Yalong Jiang, Qiulong Wei,* Qianming Huang, Yuhang Dai, Fangyu Xiong, Qidong Li, Qinyou An, Xu Xu, Zizhong Zhu, Xuedong Bai,* and Liqiang Mai*

Conversion-type anodes with multielectron reactions are beneficial for achieving a high capacity in sodium-ion batteries. Enhancing the electron/ion conductivity and structural stability are two key challenges in the development of high-performance sodium storage. Herein, a novel multidimensionally assembled nanoarchitecture is presented, which consists of V_2O_3 nanoparticles embedded in amorphous carbon nanotubes that are then coassembled within a reduced graphene oxide (rGO) network, this materials is denoted $V_2O_3 \subset C\text{-NTs} \subset rGO$. The selective insertion and multiphase conversion mechanism of V_2O_3 in sodium-ion storage is systematically demonstrated for the first time. Importantly, the naturally integrated advantages of each subunit synergistically provide a robust structure and rapid electron/ion transport, as confirmed by in situ and ex situ transmission electron microscopy experiments and kinetic analysis. Benefiting from the synergistic effects, the $V_2O_3 \subset C\text{-NTs} \subset rGO$ anode delivers an ultralong cycle life (72.3% at 5 A g^{-1} after 15 000 cycles) and an ultrahigh rate capability (165 mAh g^{-1} at 20 A g^{-1}, ≈30 s per charge/discharge). The synergistic design of the multidimensionally assembled nanoarchitecture produces superior advantages in energy storage.

S. Tan, Y. Jiang, Dr. Q. Wei, Y. Dai, F. Xiong, Q. Li, Prof. Q. An, Dr. X. Xu, Prof. L. Mai
State Key Laboratory of Advanced Technology for Materials Synthesis and Processing
International School of Materials Science and Engineering
Wuhan University of Technology
Wuhan 430070, Hubei, China
E-mail: qlwei@ucla.edu; mlq518@whut.edu.cn

Dr. Q. Wei
Department of Materials Science and Engineering
University of California Los Angeles
CA 90095-1595, USA

Dr. Q. Huang, Prof. X. Bai
Beijing National Laboratory for Condensed Matter Physics and Institute of Physics
Chinese academy of Sciences
Beijing 100190, China
E-mail: xdbai@iphy.ac.cn

Prof. Z. Zhu
Department of Physics and Institute of Theoretical Physics and Astrophysics
Xiamen University
Xiamen 361005, China

Prof. L. Mai
Department of Chemistry
University of California
Berkeley, CA 94720, USA

The ORCID identification number(s) for the author(s) of this article can be found under https://doi.org/10.1002/adma.201707122.

Sodium-ion batteries (SIBs) are a highly promising alternative to lithium-ion batteries (LIBs) for grid and large-scale energy storage systems (ESSs) owing to the abundant resources and low cost of Na.[1–3] Generally, similar to LIBs, SIBs operate through the shuttling of Na$^+$ ions between the cathode and anode during cycling.[1] However, the larger cation radius and heavier atomic weight of the Na$^+$ ion (1.02 Å and 23 g mol^{-1}), relative to those of the Li$^+$ ion (0.76 Å and 6.9 g mol^{-1}) cause sluggish ion kinetics and a high potential barrier for intercalation into the active materials.[3] Unfortunately, commercial graphite anodes deliver a very low capacity of only ≈35 mAh g^{-1} (in sodium-ion storage, which is unsuitable for practical use.[4] Recently, intercalation-type anodes, such as expanded graphite,[5] hard carbon,[6] Li$_4$Ti$_5$O$_{12}$,[7] Na$_4$Ti$_5$O$_{12}$,[8] and Na$_{0.66}$[Li$_{0.22}$Ti$_{0.78}$]O$_2$[9] have been reported to possess an enhanced sodium-ion storage capacity. However, the achieved capacities were limited to 300 mAh g^{-1} due to the limited number of sodium host sites in these anodes. Conversion-type anodes with high specific capacities, such as metal oxides,[10] metal sulfides,[11,12] and metal selenides,[13] among others,[14,15] have attracted considerable interests. However, two main challenges limit the ability of conversion-type anodes to deliver both a high rate and long-term cycling performance: (1) the structural degradation caused by the large volume change and (2) the poor rate performance owing to the low intrinsic electron and ion conductivities of the anodes.[16]

In attempts to address the abovementioned issues, previous works demonstrated that zero-dimensional (0D) nanoparticles (NPs) could accommodate the large volume changes.[17] However, self-aggregation of the NPs during repeated sodiation/desodiation processes led to inefficient electrolyte–electrode contact and increased the interface charge transfer resistance. Therefore, the unmodified NPs delivered an unsatisfactory long-term cycling stability (**Figure 1**a).[18] Two-dimensional (2D) graphene nanosheets and their assembled three-dimensional (3D) frameworks have been widely used as matrixes to relieve these issues. However, the open structures of these materials are not able to fully confine the volume changes and self-aggregation of the sodiated NPs through the weak interactions between the NPs and 2D graphene.[11] The construction of well-confined nanostructures that employ conductive 1D carbon tubular nanostructures

**ADVANCED
SCIENCE NEWS**

www.advancedsciencenews.com

**ADVANCED
MATERIALS**

www.advmat.de
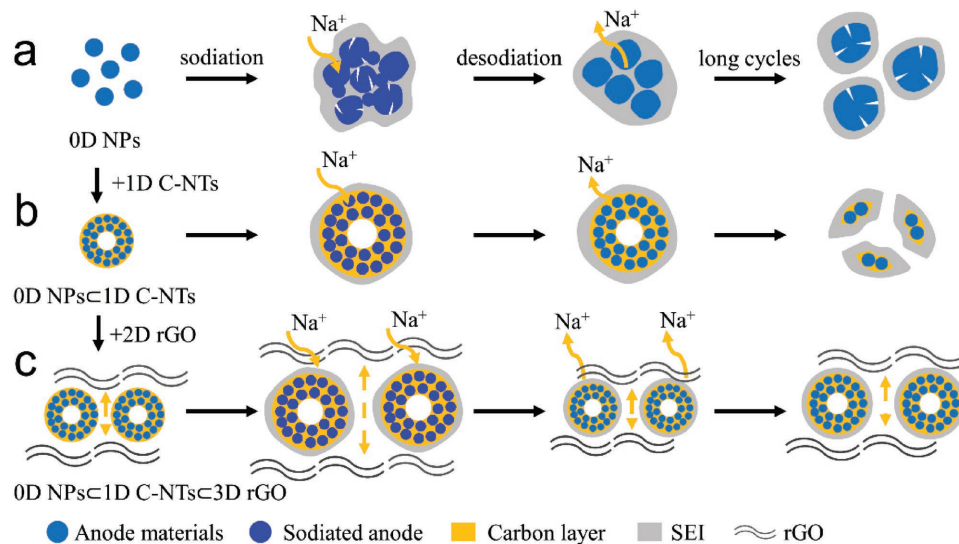
Figure 1. Schematic of the electrochemical process for three configurations of electrodes. a) 0D NPs undergo substantial structural expansion, which tends to cause extensive self-aggregation, resulting in poor cycling stability and a large irreversible capacity loss. b) 1D C-NTs provide a protective coating for 0D NPs and improve the electron transport kinetics, but cracking of the pyrolytic carbon shell occurs with increasing number of cycles, as a result of its low elasticity. c) 3D rGO as a buffering framework effectively stabilizes the 1D NTs, allowing the 1D NTs to restrict the expansion and reaggregation of 0D NPs in the long-term, leading to an ultralong cycle life and high rate performance (microscopic region of the 3D structure).

as a matrix (Figure 1b) with uniformly embedded fine NPs (0D⊂1D) has potential to substantially reduce self-aggregation of the NPs. Meanwhile, the modified electron conductivity is beneficial for obtaining a high rate capability.[19–23] In addition, the voids within the matrix provide the space needed to accommodate the repeated volume changes associated with the diffusion of ions in and out, leading to a remarkably enhanced cycling stability.[24] Nevertheless, pyrolytic amorphous carbon with a low elasticity may not be suitable for the ultralong-term (thousands of cycles) accommodation of the large volume expansion.[25,26] Therefore, introducing 2D graphene into the matrix to further assemble a novel, high-stable 0D⊂1D⊂3D structure that combines the advantages of each 0D, 1D, and 2D unit is considered to be an ideal method for delivering a remarkable electrochemical performance. However, this type of well-designed structure has rarely been reported, and the detailed relationships between the electrochemical performance and structure remain largely unexplored.[27–29]

V_2O_3 has been extensively investigated as a potential anode in LIBs due to its high theoretical capacity, abundant resources, and low cost.[30–32] Conversion-type V_2O_3 anodes with multielectron reactions could also deliver a high capacity for sodium-ion storage. Herein, we present the design of a 0D⊂1D⊂3D multidimensionally assembled nanoarchitecture made of 0D V_2O_3 NPs embedded in 1D porous carbon nanotubes (C-NTs), that are then coassembled within a 3D rGO network (V_2O_3⊂C-NTs⊂rGO) (Figure 1c). The multidimensional assembled architecture presents the following attractive advantages: (i) the 3D architecture constructed from rGO nanosheets and 1D C-NTs provides a stable buffer framework, in which the voids can buffer the swelling stress of the 1D C-NTs and the C-NTs can further restrict the inward expansion of the 0D NPs; (ii) the self-aggregation of NPs is largely reduced in the V_2O_3⊂C-NTs

structure owing to the uniform distribution of ultrafine NPs embedded in the 1D C-NT matrix; and (iii) the 1D C-NTs and 3D rGO framework provide bicontinuous electron and ion transport paths, thereby facilitating fast reaction kinetics. Benefiting from the synergistic effects between each dimensional nanostructure, the 0D⊂1D⊂3D nanoarchitecture shows greatly enhanced stability and kinetics, resulting in an ultralong lifespan of 72.3% retention at 5 A g^{-1} after 15 000 cycles and a high rate capacity of 165 mAh g^{-1} up to 20 A g^{-1}.

Synthesis and Characterization of Multidimensional V_2O_3⊂CNTs⊂rGO

The detailed assembly processes of V_2O_3⊂C-NTs⊂rGO are illustrated in **Figure 2**a. First, the VO_x nanotubes (VO_x-NTs) precursor were synthesized through the cetylamine-assisted self-scrolling method,[33,34] producing NTs with diameters ranging from 100 to 200 nm, as shown by field-emission scanning electron microscopy (SEM) (Figure 2b; Figure S1a, Supporting Information). The VO_x-NTs modified with long hydrophobic alkyl chains of cetylamine were thoroughly dispersed in alcohol, and then an aqueous dispersion of graphene oxide (GO) nanosheets (GO-NSs) was mixed in. The cationic surfactant cetyltrimethyl ammonium bromide (CTAB) was subsequently added to realize the co-assembly of the VO_x-NTs and 2D GO-NSs (VO_x-NTs⊂GO) through electrostatic interactions. After centrifugation, the mixed slurry was rapidly frozen in liquid nitrogen prior to freeze-drying. In this case, the VO_x-NTs were uniformly distributed within the GO-NS network (Figure 2c; Figure S1b, Supporting Information). After annealing in a reducing atmosphere, the cetylamine molecules were pyrolyzed and transformed to an N-doped amorphous C-NT matrix, and the GO-NSs were simultaneously reduced (denoted rGO-NSs). The VO_x-NTs were also transformed into

**ADVANCED
SCIENCE NEWS**
www.advancedsciencenews.com

**ADVANCED
MATERIALS**
www.advmat.de
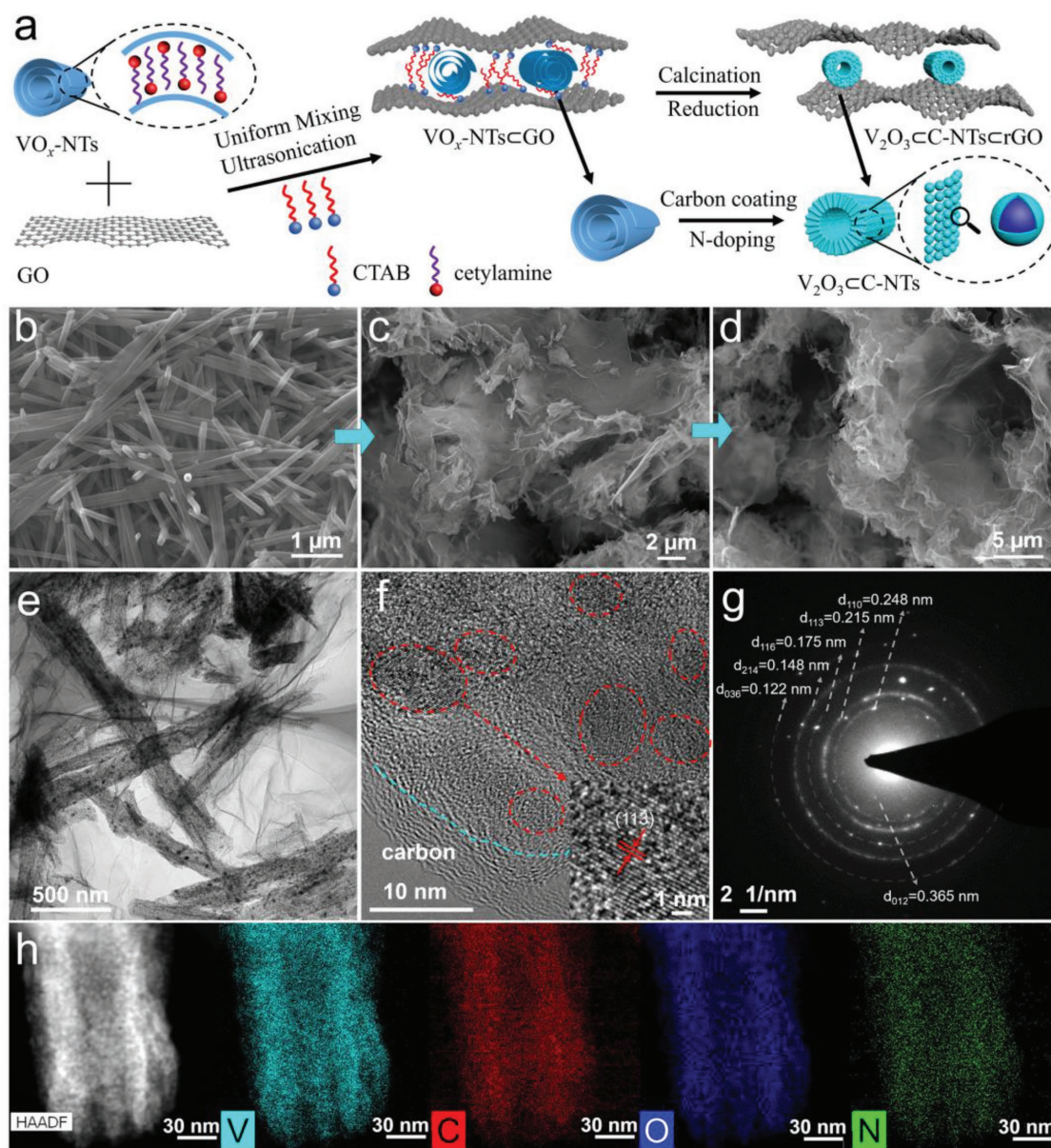
Figure 2. Synthesis and characterization of $V_2O_3 \subset$C-NTs$\subset$rGO. a) Schematic of the synthesis of $V_2O_3 \subset$C-NTs$\subset$rGO. SEM images of b) the VO_x-NTs, c) VO_x-NTs$\subset$GO, and d) $V_2O_3 \subset$C-NTs$\subset$rGO. e) TEM image of $V_2O_3 \subset$C-NTs$\subset$rGO and the corresponding f) HRTEM and g) SAED images. h) HAADF image and corresponding element maps of a single $V_2O_3 \subset$C-NT.

ultrafine V_2O_3 NPs embedded in the as-formed C-NTs (denoted $V_2O_3 \subset$C-NTs). During the thermal treatment, the size of the voids between the C-NTs and rGO-NSs was reduced, resulting in a close contact between the components. As shown in Figure 2d and Figure S1c (Supporting Information), the $V_2O_3 \subset$C-NTs are deeply embedded in the rGO network. In addition, $V_2O_3 \subset$C-NTs (Figure S2, Supporting Information), $V_2O_3 \subset$rGO and V_2O_3-NPs (Figure S3, Supporting Information) were synthesized as controls to investigate the relationship between the electrochemical performance and the structure.

Transmission electron microscopy (TEM) was used to further characterize the structure and morphology (Figure 2e–h). The $V_2O_3 \subset$C-NTs are well assembled in between rGO sheets,

while ultrafine V_2O_3 NPs are uniformly embedded in the C-NTs (Figure 2e; Figure S4, Supporting Information). After etching the V_2O_3 in the $V_2O_3 \subset$C-NTs with hydrochloric acid (Figure S5, Supporting Information), porous C-NTs are clearly observed, which further confirms that the V_2O_3 NPs are embedded in the matrix. From examination of a single $V_2O_3 \subset$C-NT, the V_2O_3 NPs are observed to be coated by a carbon layer, and their sizes range from 8 to 20 nm (Figure 2f; Figure S6, Supporting Information). The high-resolution TEM (HRTEM) image (inset of Figure 2f) further reveals the presence of a lattice fringe with an interplanar spacing of 0.218 nm, corresponding to the (113) plane of V_2O_3 (JCPDS No. 71–0342). The corresponding selected area electron diffraction (SAED)

**ADVANCED
SCIENCE NEWS**

www.advancedsciencenews.com

**ADVANCED
MATERIALS**

www.advmat.de
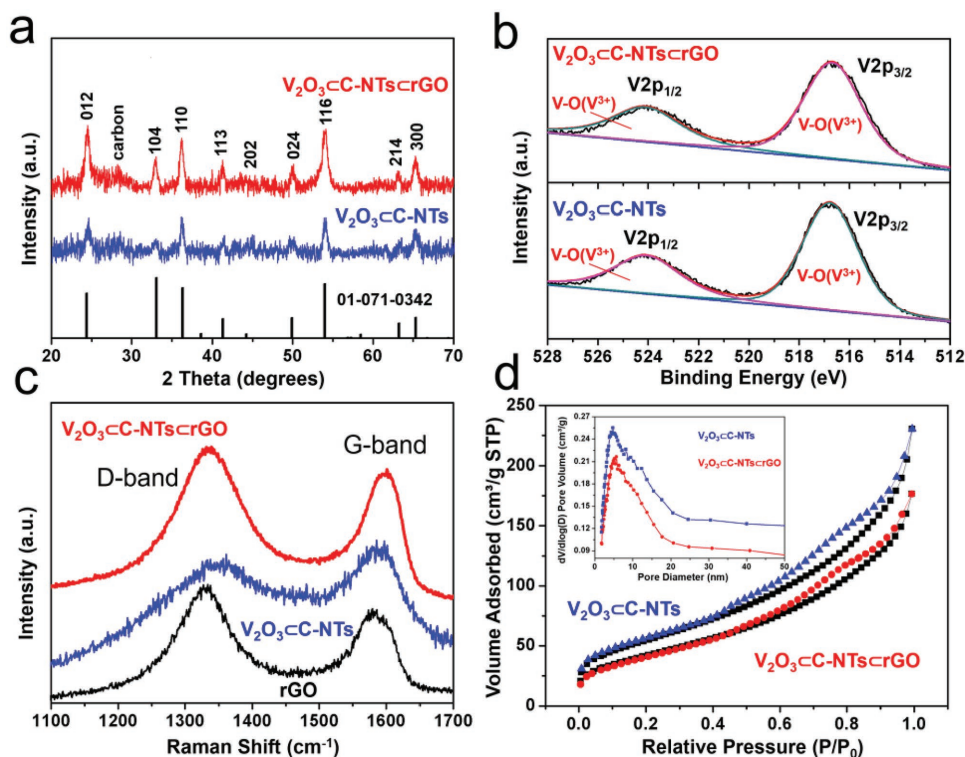
Figure 3. Phase, composition and pore structure characterization of $V_2O_3 \subset C\text{-NTs} \subset rGO$. a) Powder XRD patterns, b) V2p XPS spectra, c) Raman spectra, and d) nitrogen adsorption–desorption isotherms of $V_2O_3 \subset C\text{-NTs} \subset rGO$ and $V_2O_3 \subset C\text{-NTs}$. The inset is the corresponding pore size distribution.

pattern reveals the polycrystalline nature of the $V_2O_3 \subset C\text{-NTs}$ (Figure 2g). The high-angle annular dark-field (HAADF) image of a single $V_2O_3 \subset C\text{-NT}$ confirms the ultrafine features of the V_2O_3 NPs, and the corresponding elemental mappings show the uniform distribution of V, O, C, and N (Figure 2h). Based on CHN elemental analysis, the carbon contents of $V_2O_3 \subset C\text{-NTs} \subset rGO$ and $V_2O_3 \subset C\text{-NTs}$ are 18.0 and 11.2 wt%, respectively, indicating that the content of rGO is 6.8 wt%. The N-doping contents of $V_2O_3 \subset C\text{-NTs} \subset rGO$ and $V_2O_3 \subset C\text{-NTs}$ are 0.88 and 0.82 wt%, respectively.

The phases of the samples were identified by powder X-ray diffraction (XRD) (**Figure 3**a). All the diffraction peaks are indexed to rhombohedral V_2O_3 (JCPDS No. 71–0342, space group: $R\text{-}3c$). X-ray photoelectron spectroscopy (XPS) was used to characterize the chemical compositions and states of the two samples. The survey spectra reveal that the two samples consist of the elements V, O, N, and C (Figure S7a, Supporting Information). The V 2p core level spectra of the two samples exhibit two peaks located at 516.8 (V $2p_{3/2}$) and 524.1 eV (V $2p_{1/2}$), corresponding to the V^{3+} valence state (Figure 3b).[31,33] The N 1s peak observed at 400.5 eV is assigned to pyrrolic nitrogen, and the N-doping of the C-NTs is shown to be beneficial for increasing the electrical conductivity (Figure S7b, Supporting Information).[35] Raman spectra were recorded to further study the nature of the V_2O_3 crystals and carbon in the samples. The peaks located below 1100 cm^{-1} correspond to characteristic bonds of V_2O_3 (Figure S7c, Supporting Information). The two peaks located at ≈1340 and 1600 cm^{-1} are attributed to the D-band (disorder induced phonon mode) and G-band (graphite band), respectively, of carbon (Figure 3c).[36] The I_D/I_G

and C−C sp^3/sp^2 ratios (Figure S7e,f, Supporting Information) of the $V_2O_3 \subset C\text{-NTs}$ are 0.86 and 1.5, respectively, which indicate the partial graphitization of the C-NTs matrix. The corresponding I_D/I_G and C−C sp^3/sp^2 ratios of $V_2O_3 \subset C\text{-NTs} \subset rGO$ are 1.13 and 0.37, respectively, owing to the existence of rGO.[37] Nitrogen adsorption isotherms were generated to investigate the specific surface area (SSA) and porous structure of the samples. The Brunauer–Emmett–Teller SSAs of $V_2O_3 \subset C\text{-NTs} \subset rGO$ and $V_2O_3 \subset C\text{-NTs}$ are 151.5 and 196.0 m^2 g^{-1}, respectively. The smaller SSA of $V_2O_3 \subset C\text{-NTs} \subset rGO$ is due to the fact that some pores are encapsulated or covered by the rGO sheets. The nitrogen adsorption–desorption curves (Figure 3d) exhibit typical H3 (type-II) hysteresis, indicating the existence of slit-shaped mesopores in both samples.[38] The Barrett–Joyner–Halenda pore size distribution curves of the two samples (inset of Figure 3d) indicate that their pore sizes are within the range of 2–20 nm with an average pore size of ≈6.8 nm in both, indicating that rGO has little influence on the pore structure.

Reversible Sodium-Ion-Storage Mechanism of $V_2O_3 \subset CNTs \subset rGO$

The reversibility of a conversion-type anode is one of the most challenging properties to achieve. Nanoarchitectures with short and continuous ion/electron transport pathways provide excellent dynamic reaction properties that enhance the reversibility.[39] In this part of the study, ex situ TEM and XPS and density functional theory (DFT) calculations were undertaken to deeply investigate the reversible sodium storage mechanism of $V_2O_3 \subset C\text{-NTs} \subset rGO$ (**Figure 4**; Figures S8–S10,

**ADVANCED
SCIENCE NEWS**

www.advancedsciencenews.com

**ADVANCED
MATERIALS**

www.advmat.de
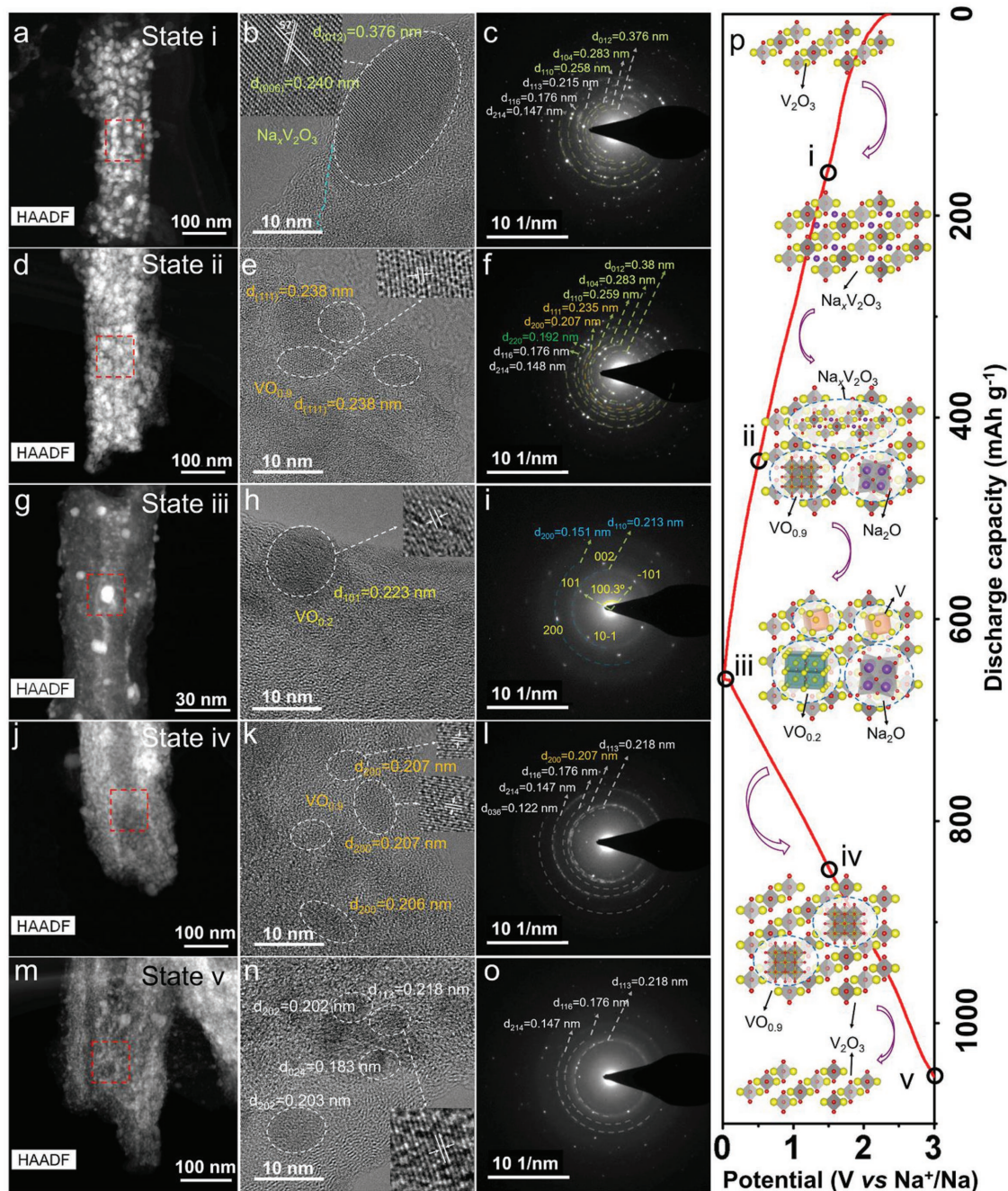
Figure 4. Na$^+$ ion storage mechanism. Structural evolution of the V$_2$O$_3$⊂C-NTs⊂rGO electrode during the sodiation and desodiation processes of the first cycles. a–o) Five states were deeply investigated: (i) discharge to 1.5 V (a–c), (ii) discharge to 0.5 V (d–f), (iii) discharge to 0.01 V (g–i), (iv) charge to 1.5 V (j–l), and (v) charge to 3.0 V (m–o). The corresponding HAADF, TEM, and SAED images of each state are also shown. The light green, green, orange, yellow, and blue annotations represent the data corresponding to Na$_x$V$_2$O$_3$, Na$_2$O, VO$_{0.9}$, VO$_{0.2}$, and V, respectively. p) First discharge–charge curve and schematic of the corresponding phase transformations of V$_2$O$_3$ at the various states.

Supporting Information). First, the ex situ HAADF image of the anode after discharged to 1.5 V (state i) shows that negligible change occurred in the morphology of C-NT (Figure 4a). The HRTEM image of the anode reveals the crystalline structure of the sodiated V$_2$O$_3$ NPs. Two interplanar spacings of 0.376 and 0.240 nm that are large than the original spacing of 0.365 and 0.233 nm correspond to the (012) and (006) planes, respectively,

of Na$_x$V$_2$O$_3$ (Figure 4b), and the angle between these planes is 57°. This result indicates that Na$^+$ ions insert into the interplanar of the (012) and (006) planes of V$_2$O$_3$ without affecting the rhombohedral phase at this step. Moreover, the SAED pattern reveals that the (012), (104), and (110) facets have expanded (Figure 4c). However, there is no distinct change in (113), (116), and (214) planes, which have small interplanar spacings.

**ADVANCED
SCIENCE NEWS**
www.advancedsciencenews.com

**ADVANCED
MATERIALS**
www.advmat.de

DFT calculations were further undertaken to explain this phenomenon (Figures S8 and S9 and Table S1, Supporting Information). The intercalation of Na^+ ions into the interplanar spacing of the (012) facet has a small binding energy or volume change (Figure S9, Sites 1–3, Supporting Information). However, when the Na^+ ions occupy the inner spaces of the (012) facet, a large volume change and serious damage to the layer structure are observed (Sites 4–6). These results demonstrate that Na^+ ions would perform a selective intercalation process depending on the exposed facets of the V_2O_3 NPs. The difficulty of some V_2O_3 NPs with small exposed facets to participate in the sodiation reaction may be due to the high energy barrier of the sodium-ion insertion process.[40] When the anode is further discharged to 0.5 V (state ii), pulverization of the V_2O_3 NPs is observed, while the carbon matrix inhibit their aggregation (Figure 4d). In this state, the (111) and (200) planes of cubic $VO_{0.9}$ (JCPDS No. 010–0313) and the (220) facet of Na_2O are observed (Figure 4e,f), indicating the occurrence of a conversion process. Interestingly, unlike the traditional conversion reaction between oxides and metal,[14] multiphase hybrid low-valent vanadium oxides are formed as intermediates in the gradual conversion reduction. During discharge to 0.01 V (state iii), most of the NPs in the C-NT matrix disintegrate into even smaller particles (Figure 4g). The HRTEM image of this state (Figure 4h) shows the (101) plane of $VO_{0.2}$ (JCPDS No. 010–0321). The related SAED pattern (Figure 4i) reveals the hybrid diffraction pattern of crystal $VO_{0.2}$ and polycrystalline metallic vanadium (JCPDS No. 089–2766). XPS experiment further verifies the occurrence of valence state changes in vanadium at 0.01 V (Figure S10b, Supporting Information). The V $2p_{3/2}$ peak can be divided into four peaks, corresponding to the V—O (V^{3+}), V—O (V^{2+}/V^+), and V^0,[41] which indicates that the V_2O_3 NPs are reduced into various low-valence oxides and vanadium metal. The $V_2O_3 \subset$C-NTs$\subset$rGO anode delivers an initial capacity of 653 mAh g^{-1} at 0.1 A g^{-1}, which is less than the theoretical capacity of 1073 mAh g^{-1} (according to 6 mol of Na^+ ion during the complete conversion reaction). The presence of trivalent and low-valent vanadium oxides suggests the conversion reaction is incomplete.

During the desodiation process, the conversion products gradually return to the $VO_{0.9}$ (Figure 4j–l) and V_2O_3 phases (Figure 4m–o; Figure S10c, Supporting Information), indicating that the multiphase conversion reaction of $V_2O_3 \subset$C-NTs$\subset$rGO is highly reversible. In addition, the structure of $V_2O_3 \subset$C-NTs$\subset$rGO is well maintained. Based on the above results, the electrochemical sodium storage mechanism of V_2O_3 is a two-step reaction (Figure 4p), as described in Equations (1) and (2).

$$V_2O_3 + x\,Na^+ + x\,e^- = Na_xV_2O_3, 1.5\,V < E < 3.0\,V \tag{1}$$

$$Na_xV_2O_3 + (6-x)\,Na^+ + (6-x)\,e^- = 3\,Na_2O + 2\,V\ 0.01\,V < E < 1.5\,V \tag{2}$$
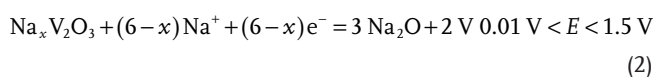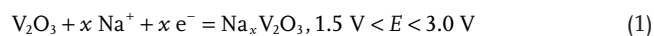
Synergistic Effects of $V_2O_3 \subset$C-NTs$\subset$rGO in Long-Term Cycling

To investigate the effects of the 1D C-NT matrix and 3D rGO framework on the structural stability, in situ TEM experiments were performed to probe the morphology changes, and ex situ SEM and TEM images were collected after long-term cycling as supplementary data. First, for the in situ TEM experiments, nanoscale sodium-ion half-cells consisting of Na metal as the anode, Na_2O as the solid electrolyte, and $V_2O_3 \subset$C-NTs or $V_2O_3 \subset$C-NTs$\subset$rGO as the cathode were assembled (**Figure 5**a,c). The dynamic reaction processes of the $V_2O_3 \subset$C-NTs and $V_2O_3 \subset$C-NTs$\subset$rGO are shown in Movies S1 and S2 of the Supporting Information, respectively. For the $V_2O_3 \subset$C-NTs, with an increase in the sodiated time, the brightness contrast of the V_2O_3 NPs changes, which is accompanied by the appearance of very small cracked pores in the polycrystalline NTs (Figure 5b; Figure S11, Supporting Information). Moreover, after 300 s and even 500 s, evident volume expansion of the sodiated $V_2O_3 \subset$C-NTs relative to pristine nanotubes. Ex situ SEM images of the $V_2O_3 \subset$C-NTs after 100, 300, and 500 cycles (Figure S12a–c, Supporting Information) further show the gradual breakage of the short nanorods and aggregation of particles with increasing number of cycles, and many V_2O_3 nanocrystals form on the surface of these nanorods and particles, leading to the loss of activity and capacity. The observated morphology changes of the $V_2O_3 \subset$C-NTs indicate that structural stability of the pyrolytic C-NTs as the sole protective matrix is still not ideal owing to its low strength and elasticity during the gradual volume variation. In comparison, during the in situ TEM observation of $V_2O_3 \subset$C-NTs$\subset$rGO (Figure 5d), the bent rGO nanosheets are observed to continually stretch with the slight expansion of the $V_2O_3 \subset$C-NTs. This phenomenon indicates that the extra rGO framework could buffer the swelling stress by the self-extension of folds to prevent fracture of $V_2O_3 \subset$C-NTs, which plays an important role in long-term repeated sodiation/desodiation processes. The multidimensional assembled $V_2O_3 \subset$C-NTs$\subset$rGO maintains the integrated 0D$\subset$1D$\subset$3D structure well, even after 500 cycles (Figure 5e,f; Figure S12d–f). Meanwhile, the integrated C-NT skeletons (obtained by etching the V_2O_3 in hydrochloric acid) largely remain intact (Figure 5h). Statistical analysis of the V_2O_3 NPs size distribution before and after 500 cycles verifies the confinement effect of the C-NT matrix (Figure 5i). The average diameters of the initial and cycled V_2O_3 NPs are 11.0 and 19.7 nm, respectively, indicating that the $V_2O_3 \subset$C-NTs$\subset$rGO favorably prevents extensive reaggregation during long-term volume changes. The Nyquist plots reveal that the increase in charge transfer resistance (R_{ct}) of $V_2O_3 \subset$C-NTs$\subset$rGO in the 1000th cycle is obviously smaller than that of the $V_2O_3 \subset$C-NTs in the 500th cycle (Figure 5j; Figure S13, Supporting Information), suggesting that the stabilizing effect of the 3D rGO frame provides a continuous electron transport path and a stable interface.

In the hierarchical $V_2O_3 \subset$C-NTs$\subset$rGO nanoarchitecture, each unit not only imparts its structural advantages, but also improves the overcomes of the other units. As the active material, the 0D V_2O_3 NPs offer a short ion diffusion distance and a large electrode/electrolyte reaction area, which intensifies the selective Na^+ ion insertion and multiphase conversion processes, leading to a higher capacity. The 1D C-NTs as the first-stage protective matrix effectively confine the expansion and aggregation of V_2O_3 NPs while also facilitating electron transport and promoting
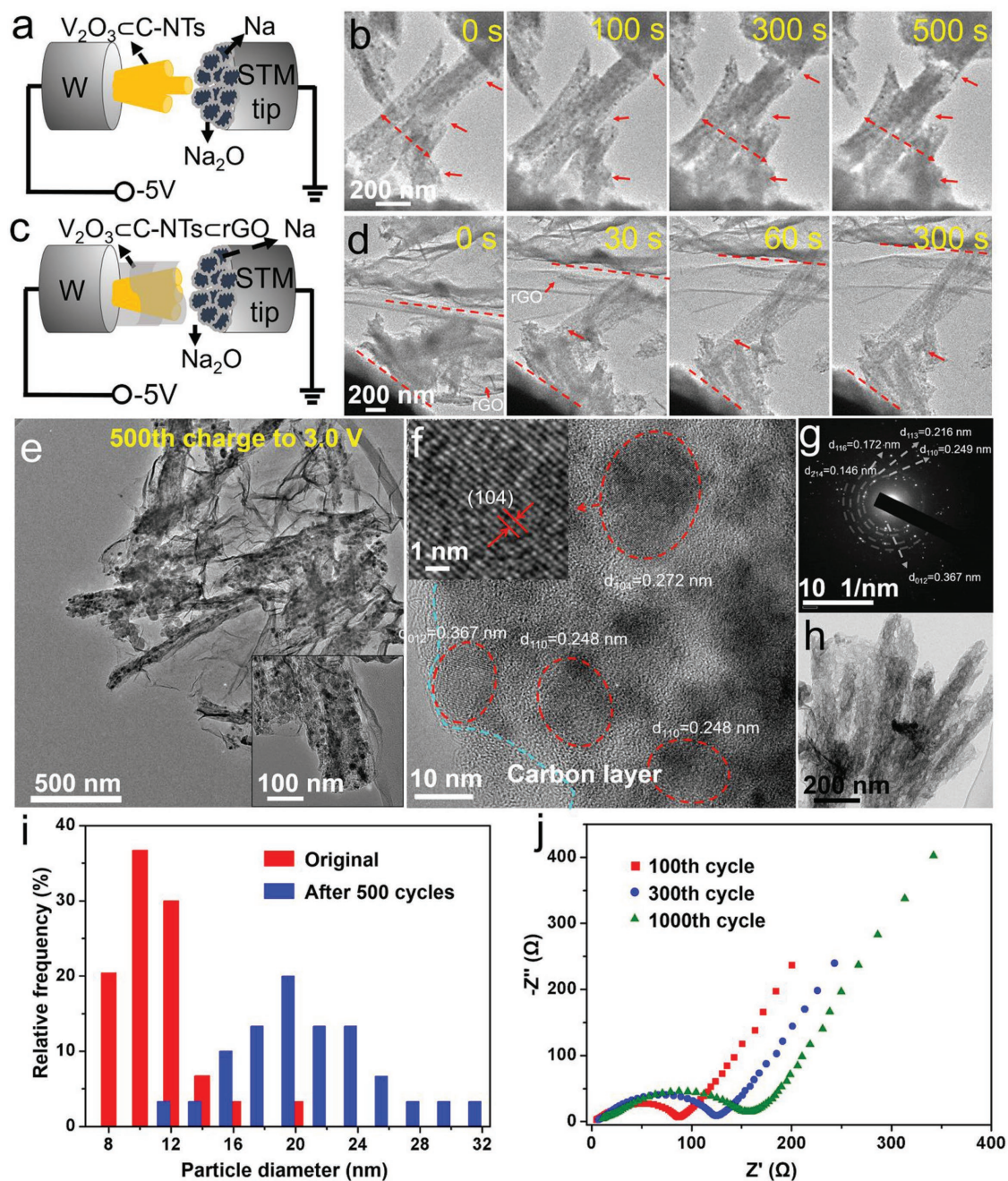
Figure 5. Synergistic effects determined by in situ TEM, ex situ SEM, and TEM experiments. Schematic and structural evolution of a,b) the $V_2O_3 \subset C$-NTs and c,d) $V_2O_3 \subset C$-NTs$\subset$rGO electrodes observed by in situ TEM experiments, respectively, during constant potential discharge at 5 V. The sodiated $V_2O_3 \subset C$-NTs undergo an evident volume expansion, and cracks from with increasing sodiation time. In comparison, during the in situ TEM observations of the $V_2O_3 \subset C$-NTs encapsulated in rGO, the bent rGO nanosheets continually stretch while the $V_2O_3 \subset C$-NTs exhibit only a little expansion during gradual sodiation. e) TEM image, f) HRTEM image, and g) corresponding SAED pattern of $V_2O_3 \subset C$-NTs$\subset$rGO after 500 cycles. h) TEM image of the carbon skeleton etched by hydrochloric acid after 500 cycles. i) Statistical analysis of the V_2O_3 NPs diameter in $V_2O_3 \subset C$-NTs$\subset$rGO before and after 500 cycles. j) Nyquist plots of $V_2O_3 \subset C$-NTs$\subset$rGO after the 100th, 300th, 1000th cycle.

the reversibility of the conversion reaction.[39] The 3D rGO as a second-stage stabilizing framework buffers the swelling stress through self-extension,[42] which allows the 1D C-NTs to protect the repeated sodiation/desodiation of the V_2O_3 NPs in the long-term. This synergy among the multidimensional nanostructures results in the highly stable and fast sodium-ion storage.

Sodium-Ion-Storage Performance

The electrochemical sodium ion storage performance of the samples was investigated by assembling coin cells (2016-type) with metallic Na as the anode. The specific capacities were calculated based on the total weight of the active material including

ADVANCED
SCIENCE NEWS
www.advancedsciencenews.com

ADVANCED
MATERIALS
www.advmat.de
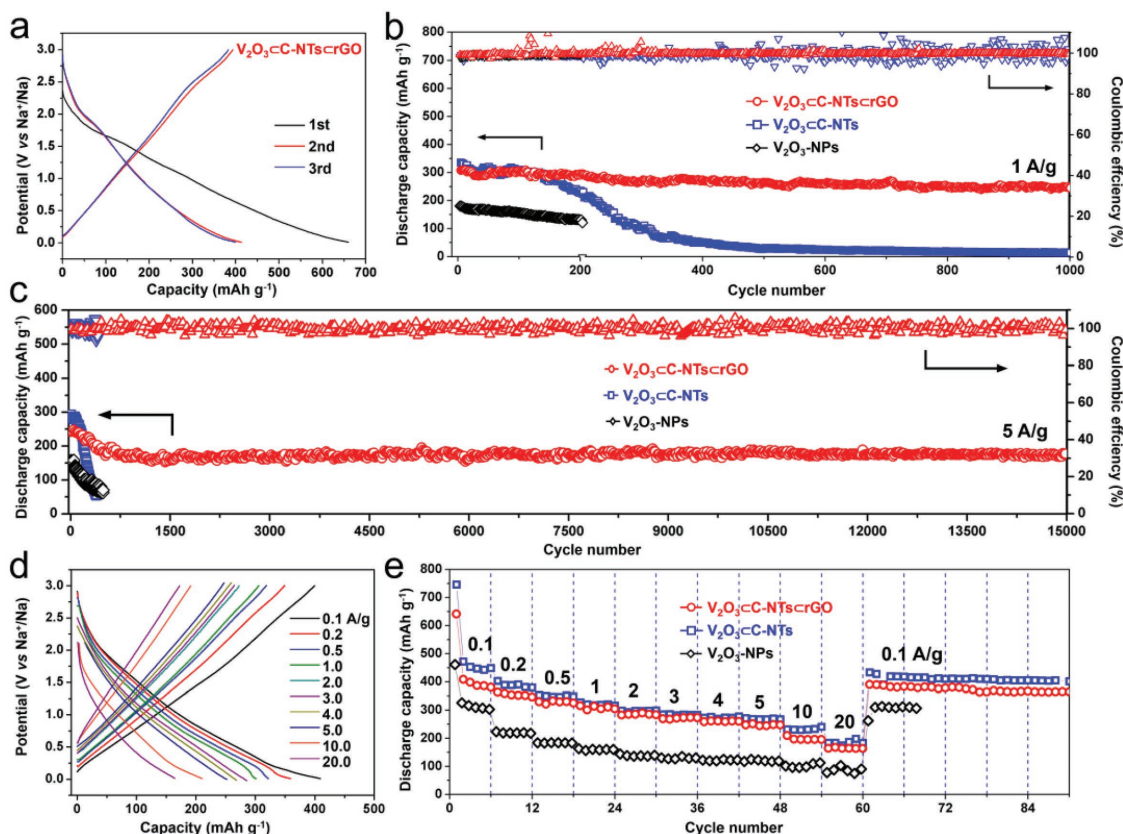
Figure 6. Sodium-ion-storage performance. a) Charge–discharge curves of the $V_2O_3 \subset$C-NTs$\subset$rGO anode from 0.01 to 3.0 V at 0.1 A g^{-1} in different cycles. Cycling performance and corresponding coulombic efficiency of $V_2O_3 \subset$C-NTs$\subset$rGO, $V_2O_3 \subset$C-NTs, and V_2O_3-NPs at b) 1 A g^{-1} and c) at high rate of 5.0 A g^{-1} (initially activated at 0.1 A g^{-1} for 3 cycles). d,e) Rate performance of the three samples at various current densities.

the carbon matrix, while the capacity contribution of this matrix is limited (Figure S14, Supporting Information).[43,44] The charge–discharge curves (**Figure 6**a; Figure S15, Supporting Information) show that the initial discharge/charge capacities of $V_2O_3 \subset$C-NT$\subset$rGO, $V_2O_3 \subset$C-NTs, and V_2O_3-NPs are 653/401, 742/445, and 457/306 mAh g^{-1}, respectively, with coulombic efficiencies of 61.4%, 60.0%, and 67.0%. The first irreversible capacity loss results from deteriorated decomposition of the electrolyte on the high-surface-area carbon in the composites.[39] The high specific capacity of $V_2O_3 \subset$C-NTs$\subset$rGO is superior to that of many previously reported SIB anodes, such as hollow carbon spheres,[45] FeS$_2$,[17] VO$_2$/rGO,[46] MoS$_2$/rGO,[47] and so forth. More importantly, $V_2O_3 \subset$C-NT$\subset$rGO exhibits a good cycling retention of 87% at 0.1 A g^{-1} (Figure S16, Supporting Information).

The cycling performance at 1 A g^{-1} (Figure 6b) shows the $V_2O_3 \subset$C-NTs$\subset$rGO anode has the best cyclability among the three samples. The $V_2O_3 \subset$C-NTs$\subset$rGO anode delivers a high capacity retention of 80.7% after 1000 cycles. However, the $V_2O_3 \subset$C-NTs anode maintains a stable capacity for only the initial 100 cycles and subsequently displays rapid capacity fading, which is consistent with the ex situ SEM results (Figure S12, Supporting Information). $V_2O_3 \subset$rGO with an open rGO frame also does not exhibit good cycling stability (Figure S17, Supporting Information). To evaluate the cycling performance under a high current response, faster charge and discharge

tests were also carried out at 5.0 A g^{-1} (Figure 6c). The $V_2O_3 \subset$C-NTs$\subset$rGO anode exhibits a high capacity of 175 mAh g^{-1} after 15 000 cycles, indicating a high capacity retention of 72.3%. Meanwhile, little capacity loss occurs between the 700th and 15 000th cycles. By contrast, the $V_2O_3 \subset$C-NTs and V_2O_3-NPs suffer extensive capacity fading within a few hundred cycles (Figure 6c; Figure S18, Supporting Information). These results verify that the 3D rGO frame effectively prevents the degradation of the 1D C-NTs during long-term cycling, enabling the C-NTs to confine the expansion and aggregation of the V_2O_3 NPs in the long term. To the best of our knowledge, such an ultralong cycle life at a high rate is much better than that in many previous reports on conversion-type anodes (the relevant reports are cited in Table S2 of the Supporting Information).

The $V_2O_3 \subset$C-NTs$\subset$rGO anode also shows a considerably enhanced rate performance. The rate capacities and charge–discharge curves of the three samples from 0.1 to 20 A g^{-1} are shown in Figure 6d and Figure S19 (Supporting Information), respectively. When the current density reaches 0.1, 0.5, 1, 5, 10, and even 20 A g^{-1}, $V_2O_3 \subset$C-NTs$\subset$rGO delivers a high discharge capacity of 408, 330, 310, 241, 210, and 165 mAh g^{-1}, respectively. The high rate response at 20 A g^{-1} represents an ultrafast charge and discharge time of ≈30 s. In addition, after subjecting the electrode to a rapid change in the rate, the $V_2O_3 \subset$C-NTs$\subset$rGO still exhibits a discharge capacity of 390 mAh g^{-1} (95.6% of the capacity is recovered), indicating the

good rate stability of the electrode. Meanwhile, $V_2O_3 \subset$ C-NTs also exhibit good rate performance and deliver a slightly higher capacity than $V_2O_3 \subset$ C-NTs $\subset$ rGO owing to its higher V_2O_3 content. However, the V_2O_3-NPs without the carbon coating deliver only low capacities at the various rates. To further explain the high rate performance, the enhanced transfer kinetics were examined by distinguishing the Na^+ ion storage capacities. We collected cyclic voltammetry curves of the $V_2O_3 \subset$ C-NTs $\subset$ rGO, $V_2O_3 \subset$ C-NTs, V_2O_3-NPs, and V_2O_3-bulk electrodes with increasing scan rates (Figures S20 and S21, Supporting Information). Quantitative analysis of the results indicates that the decrease in the crystal size effectively suppresses the diffusion-controlled conversion reaction and largely enhances the Na^+ ion storage pseudocapacitive behavior (detailed analysis is provides in the Supporting Information).[48]

In summary, we present a multidimensionally assembled nanoarchitecture composed of 0D V_2O_3 NPs embedded in 1D C-NTs and further coassembled within a 3D rGO network. A demonstrated by in situ and ex situ TEM observations, the 0D$\subset$1D$\subset$3D nanoarchitecture exhibits unique synergistic effects, in which each unit exerts its own advantages and overcomes the deficiencies of the other units. This synergy produces an ultralong cyclic retention of 72.3% at 5 A g^{-1} after 15 000 cycles and a high rate capacity of 165 mAh g^{-1} up to 20 A g^{-1} for sodium ion storage. A reversible selective insertion and multiphase conversion sodium-ion-storage mechanism is also systematically investigated and provides strong theoretical support for the design of high-performance V_2O_3 SIB anodes. The present functional multidimensionally assembled 3D model with integrated functions is the future research direction toward the next generation of electrical energy storage devices, and we believe it will exhibit more unique properties for expanding the applications.

Supporting Information

Supporting Information is available from the Wiley Online Library or from the author.

Acknowledgements

Conflict of Interest

The authors declare no conflict of interest.

Keywords

[1] C. J. Wook, D. Aurbach, *Nat. Rev. Mater.* **2016**, *1*, 16013.
[2] L. Dominique, J. M. Tarascon, *Nat. Chem.* **2015**, *7*, 19.
[3] N. Yabuuchi, K. Kubota, M. Dahbi, S. Komaba, *Chem. Rev.* **2014**, *114*, 11636.
[4] S. W. Kim, D. H. Seo, X. Ma, G. Ceder, K. Kang, *Adv. Energy Mater.* **2012**, *2*, 710.
[5] Y. Wen, K. He, Y. J. Zhu, F. D. Han, Y. H. Xu, I. Matsuda, Y. Ishii, J. Cumings, C. S. Wang, *Nat. Commun.* **2014**, *5*, 4033.
[6] Y. Cao, L. Xiao, M. L. Sushko, W. Wang, B. Schwenzer, J. Xiao, Z. Nie, L. V. Saraf, Z. Yang, J. Liu, *Nano Lett.* **2012**, *12*, 3783.
[7] Y. Sun, L. Zhao, H. L. Pan, X. Lu, L. Gu, Y. S. Hu, H. Li, M. Armand, Y. C. Ikuhara, L. Q. Chen, X. J. Huang, *Nat. Commun.* **2013**, *4*, 1870.
[8] P. J. Naeyaert, M. Avdeev, N. Sharma, H. B. Yahia, C. D. Ling, *Chem. Mater.* **2014**, *26*, 7067.
[9] Y. S. Wang, X. Q. Yu, S. Y. Xu, J. M. Bai, R. j. Xiao, Y. S. Hu, H. Li, X. Q. Yang, L. Q. Chen, X. J. Huang, *Nat. Commun.* **2013**, *4*, 2365.
[10] N. Zhang, X. P. Han, Y. C. Liu, X. F. Hu, Q. Zhao, J. Chen, *Adv. Energy Mater.* **2015**, *5*, 1401123.
[11] B. H. Qu, C. Ma, G. Ji, C. H. Xu, J. Xu, Y. S. Meng, T. H. Wang, J. Y. Lee, *Adv. Mater.* **2014**, *26*, 3854.
[12] Y. Denis, P. V. Prikhodchenko, C. W. Mason, S. K. Batabyal, J. Gun, S. Sladkevich, A. G. Medvedev, O. Lev, *Nat. Commun.* **2013**, *4*, 2922.
[13] K. Zhang, Z. Hu, X. Liu, Z. Tao, J. Chen, *Adv. Mater.* **2015**, *27*, 3305.
[14] F. Klein, B. Jache, A. Bhide, P. Adelhelm, *Phys. Chem. Chem. Phys.* **2013**, *15*, 15876.
[15] W. Luo, F. Shen, C. Bommier, H. Zhu, X. Ji, L. Hu, *Acc. Chem. Res.* **2016**, *49*, 231.
[16] H. Zhu, Z. Jia, Y. Chen, N. Weadock, J. Wan, O. Vaaland, X. Han, T. Li, L. Hu, *Nano Lett.* **2013**, *13*, 3093.
[17] M. Walter, T. Zünd, M. Kovalenko, *Nanoscale* **2015**, *7*, 9158.
[18] Z. S. Wu, W. Ren, L. Wen, L. Gao, J. Zhao, Z. Chen, G. Zhou, F. Li, H. M. Cheng, *ACS Nano* **2010**, *4*, 3187.
[19] C. Niu, J. Meng, X. Wang, C. Han, M. Yan, K. Zhao, X. Xu, W. Ren, Y. Zhao, L. Xu, Q. J. Zhang, D. Y. Zhao, L. Q. Mai, *Nat. Commun.* **2015**, *6*, 7402.
[20] C. B. Zhu, X. K. Mu, P. A. van Aken, Y. Yu, J. Maier, *Angew. Chem., Int. Ed.* **2014**, *53*, 2152.
[21] L. Wu, X. Hu, J. Qian, F. Pei, F. Wu, R. Mao, X. Ai, H. Yang, Y. Cao, *Energy Environ. Sci.* **2014**, *7*, 323.
[22] Y. M. Chen, X. Y. Yu, Z. Li, U. Paik, X. W. Lou, *Sci. Adv.* **2016**, *2*, e1600021.
[23] Q. L. Wei, F. Y. Xiong, S. S. Tan, L. Huang, E. H. Lan, B. Dunn, L. Mai, *Adv. Mater.* **2017**, *29*, 1602300.
[24] H. Wu, G. Chan, J. W. Choi, Y. Yao, M. T. McDowell, S. W. Lee, A. Jackson, Y. Yang, L. Hu, Y. Cui, *Nat. Nanotechnol.* **2012**, *7*, 310.
[25] Y. Li, K. Yan, H.-W. Lee, Z. Lu, N. Liu, Y. Cui, *Nat. Energy* **2016**, *1*, 15029.
[26] H. Jiang, Y. Hu, S. Guo, C. Yan, P. S. Lee, C. Li, *ACS Nano* **2014**, *8*, 6038.

**ADVANCED
SCIENCE NEWS**

www.advancedsciencenews.com

**ADVANCED
MATERIALS**

www.advmat.de

[27] H. Y. He, W. Fu, H. T. Wang, H. Wang, C. H. Jin, H. J. Fan, Z. Liu, *Nano Energy* **2017**, *34*, 449.

[28] R. Raccichini, A. Varzi, S. Passerini, B. Scrosati, *Nat. Mater.* **2015**, *14*, 271.

[29] C. B. Zhu, X. K. Mu, P. A. van Aken, J. Maier, Y. Yu, *Adv. Energy Mater.* **2015**, *5*, 1401170.

[30] L. X. Zeng, C. Zheng, J. C. Xi, H. L. Fei, M. D. Wei, *Carbon* **2013**, *62*, 382.

[31] L. Jiang, Y. Qu, Z. Ren, P. Yu, D. Zhao, W. Zhou, L. Wang, H. Fu, *ACS Appl. Mater. Interfaces* **2015**, *7*, 1595.

[32] X. H. Xia, D. L. Chao, Y. Q. Zhang, J. Y. Zhan, Y. Zhong, X. L. Wang, Y. D. Wang, Z. X. Shen, J. P. Tu, H. J. Fan, *Small* **2016**, *12*, 3048.

[33] Q. L. Wei, S. S. Tan, X. Y. Liu, M. Y. Yan, F. C. Wang, Q. D. Li, Q. Y. An, R. M. Sun, K. N. Zhao, H. G. Wu, L. Q. Mai, *Adv. Funct. Mater.* **2015**, *25*, 1773.

[34] X. Zhou, G. Wu, G. Gao, J. Wang, H. Yang, J. Wu, J. Shen, B. Zhou, Z. Zhang, *J. Phys. Chem. C* **2012**, *116*, 21685.

[35] D. Deng, X. Pan, L. Yu, Y. Cui, Y. Jiang, J. Qi, W.-X. Li, Q. Fu, X. Ma, Q. Xue, *Chem. Mater.* **2011**, *23*, 1188.

[36] Q. An, F. Lv, Q. Liu, C. Han, K. Zhao, J. Sheng, Q. Wei, M. Yan, L. Mai, *Nano Lett.* **2014**, *14*, 6250.

[37] Q. D. Li, Q. L. Wei, J. Z. Sheng, M. Y. Yan, L. Zhou, W. Luo, R. M. Sun, L. Q. Mai, *Adv. Sci.* **2015**, *2*, 1500284.

[38] R. Rakhi, W. Chen, D. Cha, H. Alshareef, *Nano Lett.* **2012**, *12*, 2559.

[39] S. Hao, X. Shen, M. Tian, R. C. Yu, Z. X. Wang, L. Q. Chen, *Nano Energy* **2017**, *41*, 217.

[40] Y. D. Mo, Q. Ru, J. F. Chen, X. Song, L. Y. Guo, S. J. Hua, S. M. Peng, *J. Mater. Chem. A* **2015**, *3*, 19765.

[41] G. Silversmit, D. Depla, H. Poelman, G. B. Marin, R. De Gryse, *J. Electron Spectrosc.* **2004**, *135*, 167.

[42] Y. L. Zhao, J. G. Feng, X. Liu, F. C. Wang, L. F. Wang, C. W. Shi, L. Huang, X. Feng, X. Y. Chen, L. Xu, M. Y. Yan, Q. J. Zhang, X. D. Bai, H. A Wu, L. Q. Mai, *Nat. Commun.* **2014**, *5*, 4565.

[43] J. T. Xu, M. Wang, N. P. Wickramaratne, M. Jaroniec, S. X. Dou, L. M. Dai, *Adv. Mater.* **2015**, *27*, 2042.

[44] Y. J. Yang, D. M. Tang, C. Zhang, Y. H. Zhang, Q. F. Liang, S. M. Chen, Q. H. Weng, M. Zhou, Y. M. Xue, J. W. Liu, J. H. Wu, Q. H. Cui, C. Lian, G. L. Hou, F. L. Yuan, Y. S. Bando, D. Golberg, X. Wang, *Energy Environ. Sci.* **2017**, *10*, 979.

[45] K. Tang, L. J. Fu, R. J. White, L. H. Yu, M. M. Titirici, M. Antonietti, J. Maier, *Adv. Energy Mater.* **2012**, *2*, 873.

[46] G. He, L. Li, A. Manthiram, *J. Mater. Chem. A* **2015**, *3*, 14750.

[47] L. David, R. Bhandavat, G. Singh, *ACS Nano* **2014**, *8*, 1759.

[48] H. S. Kima, J. B. Cookb, S. H. Tolberta, B. Dunn, *J. Electrochem. Soc.* **2015**, *162*, A5083.